PHILOSOPHICAL TRANSACTIONS A

royalsocietypublishing.org/journal/rsta

Research

Cite this article: Ehrenfeucht S, Dow C. 2026 Impacts of bed topography resolution on sea-level rise projections from coupled subglacial hydrology and ice dynamics for Thwaites Glacier, Antarctica. *Phil. Trans. R. Soc. A* **384**: 20240545.
https://doi.org/10.1098/rsta.2024.0545

Received: 4 July 2025
Accepted: 2 September 2025

One contribution of 16 to a Theo Murphy meeting issue 'Next generation ice-sheet bed measurements'.

Subject Areas:
glaciology

Keywords:
bed topography, subglacial hydrology, sea-level rise, Thwaites Glacier, glacier modelling, Antarctic Ice Sheet

Author for correspondence:
Shivani Ehrenfeucht
e-mail:
shivani.leigh.ehrenfeucht@pik-potsdam.de

Electronic supplementary material is available online at https://doi.org/10.6084/m9.figshare.c.8375226.

THE ROYAL SOCIETY PUBLISHING

Impacts of bed topography resolution on sea-level rise projections from coupled subglacial hydrology and ice dynamics for Thwaites Glacier, Antarctica

Shivani Ehrenfeucht[1,2] and Christine Dow[2]

[1]Potsdam Institute for Climate Impact Research (PIK) e V, Potsdam, Brandenburg, Germany
[2]Department of Geography and Environmental Management, University of Waterloo, Waterloo, Ontario, Canada

SE, 0000-0001-7012-391X

Ice-sheet models require explicit knowledge of the underlying bed. However, much remains unknown regarding the subglacial environment owing to difficulties associated with measuring it. Extensive radar surveys have been conducted across Antarctica, but the requirement of full-coverage bed topography for models necessitates interpolation over gaps between existing observations, which often span kilometres or more. Advances in modelling capabilities now allow for the application of dynamic coupling between subglacial hydrology and ice dynamics in models of Antarctica. While a bed resolution of approximately 1 km is recommended for modelling Antarctic ice dynamics, it has been suggested that finer spatial resolutions are necessary to resolve subglacial water flow. We use a coupled model configuration to generate projections of glacier evolution, including the subglacial hydrologic system, for Thwaites Glacier, West Antarctica, initiated with several different bed topographies. We find that the specific bed topography has a first-order control on accumulated mass loss, but that final sea-level rise does not scale with bed resolution. We also find that coupling between subglacial hydrology and ice dynamics results in faster mass loss. Our results underscore the importance of continued high-resolution topography mapping and

suggest that current projections may underestimate uncertainty linked to unresolved bed features.

This article is part of the Theo Murphy meeting issue 'Next generation ice-sheet bed measurements'.

1. Introduction

Bed topography exerts a critical control on glacier and ice-sheet dynamics by governing ice flow [1,2] and grounding line behaviour [3,4]. High-resolution bed topography data reveal complex subglacial landscapes, including narrow troughs, overdeepenings and pinning points, which strongly influence the dynamic response of marine-terminating glaciers to ocean thermal forcing [5]. However, full-coverage bed maps of Antarctica still contain many regions that rely on interpolation between data that exceed 50 km between survey lines, limiting the accuracy of model projections of future ice-sheet behaviour in less constrained regions [6,7].

Grounding line migration is highly dependent on bed features that may be unresolved in coarser datasets [8]. Retreat past a stable grounding line position can initiate marine ice-sheet instability, a self-reinforcing, positive feedback wherein initial grounding line retreat on to a retrograde slope can destabilize marine ice sheets [9,10]. The initial retreat results in thicker ice at the grounding line, affecting ice flux across the grounding line, which is highly dependent on ice thickness [11]. This induces faster ice flow and thinning, which then amplifies the initial retreat. However, even relatively small features in the bed can help to stabilize the glacier, slow down retreat and potentially prevent extensive mass loss. Elevated bed features may act as pinning points, stabilizing the grounding line [12]. Even small-scale roughness in the bed topography is associated with variation in ice flow behaviour attributed to increased basal friction [13]. Additional uncertainties about the physical properties of the bed and the interactions of physical systems at the critical ice–bed interface compound the uncertainties associated with existing basal topography datasets in model outputs.

Subglacial hydrology in Antarctica plays an important role in modulating ice flow dynamics by influencing basal sliding and the distribution of subglacial discharge across the grounding line [2,14]. Meltwater at the ice–bed interface generated by geothermal and frictional heating forms a dynamic drainage system linking distributed cavities of meltwater to a channelized network of subglacial rivers [15,16]. Distributed meltwater at the bed reduces effective pressure, the balance between ice overburden pressure and basal water pressure, facilitating ice flow, particularly in fast-flowing ice streams and outlet glaciers [17]. The spatial and temporal variability of subglacial water routing can lead to changes in ice flow behaviours, including ice stream switching and surge-like activity. Recent work has also indicated that subglacial hydrology can directly influence glacier stability and evolution: subglacial discharge can accelerate grounding line retreat and mass loss [18], while basal water may facilitate seawater intrusion kilometres upstream, increasing basal melt rates in the grounding zone [19]. Previous modelling has shown extensive networks of subglacial channels below many of the Antarctic ice streams [20–22]. Moreover, active subglacial lakes and episodic drainage events have been observed beneath the Antarctic Ice Sheet, demonstrating that the subglacial hydrology system is highly dynamic despite the lack of surface meltwater input to the bed [23,24]. Understanding and accurately representing subglacial hydrology is therefore essential for improving projections of ice-sheet behaviour and its contribution to sea-level rise. Despite this, most ice dynamic models utilize simplified parametrizations of the subglacial pressure system to drive basal friction calculations (e.g. [25]). However, recent efforts to include more realistic subglacial hydrology in ice dynamic modelling of Greenland [26–29] and Antarctica [18,30,31] have demonstrated that the basal parametrizations play a key role in altering ice dynamic behaviour.

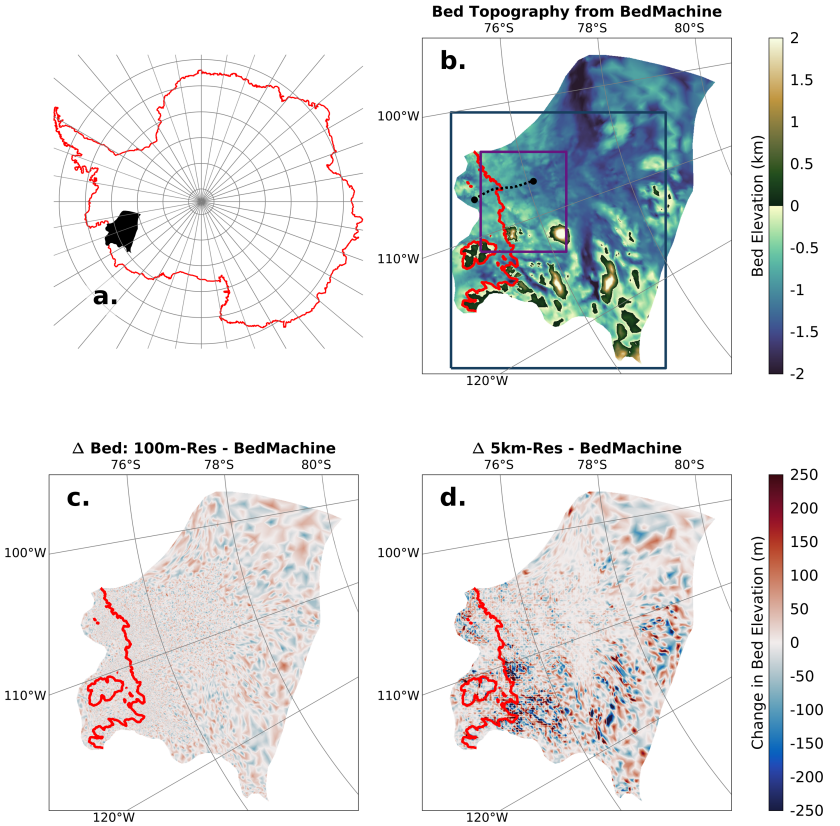

Figure 1. (a) Outline of the Antarctic Ice Sheet with our model domain shown in black. (b) Bed topography from BedMachine Antarctica v. 3 [6], with boxes indicating map extent for figure 2 and 4 (purple box) and figure 5 (blue box). The flowline used in figure 4 is shown in black (dashed line). Change in bed topography elevation for (c) the high-resolution 100 m bed topography and (d) the low-resolution 5 km bed topography variation. The red line in (b–d) indicates the grounding line location obtained from assumed hydrostatic equilibrium based on BedMachine ice geometry.

Thwaites Glacier, West Antarctica, is the widest glacier on Earth, with a 120 km grounding line [32] and has an ice velocity of over 2000 m a^{-1} [33]. Observations of rapid change of Thwaites over recent years have included thinning [34,35], ice acceleration [36,37] and rapid grounding line retreat [38,39]. A total collapse of Thwaites could raise sea levels by 65 cm [6] and destabilize the West Antarctic Ice Sheet [40], which, in conjunction with the observed changes, has made the glacier a focal point of study over recent years. Observations of subglacial hydrology are difficult to obtain and are limited or non-existent for many Antarctic glaciers. However, extensive radar surveys of Thwaites provide evidence of an active subglacial hydrological system that influences the dynamics of the glacier. Large and connected active subglacial lakes were identified after a drainage event in 2014 [41]. Recently, 27 additional active subglacial lakes were discovered [42]. Both of these studies note a change in velocity near the grounding line following lake drainage events, but do not conclusively link the two. However, the additional water released during these drainage events coincides with a near doubling of basal melt rates, which led to thinning at the grounding line and retreat [43], indicating that changes to the subglacial hydrologic system may trigger changes in the glacier dynamics.

Here, we examine how bed topography resolution influences modelled ice dynamics and sea-level contributions for Thwaites over the next several centuries, using several representations of the subglacial hydrological system. We project ice mass change to the year 2300 and analyse the effect of using bed topographies of varying spatial resolutions to represent the subglacial

environment. We discuss implications for sea-level rise projections both from topographical representations and from applying coupling between the hydrology and ice dynamic systems.

2. Methodology

To examine potential future evolutions of Thwaites Glacier, we use the Ice-sheet and Sea-level System Model (ISSM; [44]). ISSM is a state-of-the-art numerical model that integrates a range of physical processes within a finite-element framework, enabling the use of unstructured meshes with variable spatial resolution. Our mesh resolution ranges between 125 m close to the grounding line and 16 km in the slower moving regions of the glacier towards the ice divide (electronic supplementary material, fig. S1). In regions where the surface velocity is greater than 100 m a^{-1}, we limit the element size in the mesh to 2.5 km or smaller.

Ice surface elevation, bed topography and ice extent are obtained from BedMachine Antarctica v3 [6], and the two-dimensional shelfy-stream approximation for ice flow [45] is employed. We initialize the model using inversion methods (e.g. [46]) to establish the initial ice stiffness and the friction coefficient based on minimizing the misfit between modelled surface velocity and satellite observations [33]. In all simulations, a regularized Coulomb friction law is employed [47], and details pertaining to the inversion algorithm can be found in the electronic supplementary material.

Initially, two models of Thwaites are parametrized for use in our experiments. The first uses a common approximation of effective pressure employed in ice-sheet models [25,48–53] where basal water pressure is calculated under the assumption of perfect connectivity to the ocean: $N = \rho_i g H + \rho_w g z$, where ρ_i and ρ_w are the densities of ice and ocean water, respectively, g is the gravitational constant and H and z correspond to ice thickness and bed elevation, respectively (electronic supplementary material, fig. S2*a*). This approximation assumes that, for a basal environment that is well connected to the ocean everywhere, water pressure can be calculated based on bed elevation relative to sea level alone, without consideration of meltwater sources or water flow in the basal environment [54]. In our second parametrization of Thwaites (electronic supplementary material, fig. S2*b*), we apply effective pressure from steady-state, present-day subglacial hydrology modelling of the Antarctic Ice Sheet [55]. Friction inversions are conducted for both effective pressure fields (see electronic supplementary material, fig. S4), and subsequent model initialization steps are conducted in parallel for the two model versions, i.e. one model initialized using effective pressure from the perfect ocean connectivity (POC) assumption (N_POC) and the other using modelled effective pressure (N_modelled).

We next extrude both models into three dimensions and use ISSM's thermal module to solve for steady-state ice temperature and basal melt rates of grounded ice (see electronic supplementary material, fig. S5) following established methodology [51,56]. Basal temperature is used to calculate ice rheology factor B at the base of the ice following the temperature–ice viscosity relationship [54]. We use the vertically integrated ice temperature to calculate the rheology factor B in the collapsed two-dimensional shallow-shelf approximation model (electronic supplementary material, fig. S6). Rheology calculated from the thermal model ice temperature results replaces the initial field calculated from the inversions. Basal rheology and grounded ice melt rates are both fields utilized by the subglacial hydrology model, while ISSM requires the vertically integrated temperature and rheology fields to calculate ice dynamics in the two-dimensional mass balance and stress balance equations. The final model is not thermomechanically coupled, as the glacier drainage system (GlaDS) cannot yet be used in conjunction with the higher-order model in a coupled framework. Instead, we use the thermal model results as static inputs.

(a) Climate forcing data

We use climate and ocean forcing generated from the Community Earth System Model (CESM2) to force our transient model simulations to the year 2300 (electronic supplementary material, fig. S7).

These datasets were processed for use in the Ice Sheet Model Intercomparison Project for CMIP6 (ISMIP6; [57]), and we chose one high-emissions future warming scenario to drive our models: SSP 5-8.5. Antarctica is relatively stable under low-emissions scenarios in many of the ISMIP6 model simulations, with some models in the ensemble showing an accumulative gain in mass by the year 2300. ISMIP6 results for scenario SSP 5-8.5 show a stable grounding line at Thwaites that remains near its present-day position for half of the contributing models by the end of the projection in year 2300 [58]. We choose to use the high-emissions scenario in our experiments specifically because we are interested in examining differences in potential retreat behaviour that may be caused by specific choices made during model initialization regarding how to represent the basal environment. The high-emissions scenario is more likely to initiate retreat and mass loss, and larger perturbations in the forcing data may magnify changes owing to differences in the model initialization. For atmospheric forcing, we apply surface mass balance (SMB) anomalies, with respect to the 1995–2014 reference period, obtained from the CESM2 dataset. SMB anomalies are added to a higher-resolution dataset of present-day SMB obtained from the regional atmospheric climate model (RACMO2.3; [59]).

Ocean-driven melt rates for floating ice are calculated using PICOP [60], which combines the two-dimensional box model PICO [61] and a buoyant plume melt parametrization [62]. PICO calculates sub-ice shelf melt rates based on vertical overturning within the ice shelf cavity and the lateral transport of heat and salt. The buoyant plume parametrization adds the effect of grounding line depth and the local slope of the ice shelf base into the melt rate calculation. PICOP is forced by basin-averaged, far-field ocean temperature and salinity. PICOP was chosen for our experiments owing to its fast computational time and its ability to generally reproduce the spatial pattern in ice shelf melt rates calculated from satellite observations in this region [60]. We use an overturning strength coefficient of 10^6 m^3 s^{-1} and turbulent temperature exchange velocity (γ_T) of 2×10^{-5} m s^{-1}, which are tuned to produce a good match to satellite-derived ice shelf melt rates [63,64], without initiating extensive grounding line retreat past observed positions in recent years [39] during a 15 year model relaxation period. Initial ice shelf melt rates can be seen in electronic supplementary material, fig. S8.

(b) Variation of bed topography resolution

Bed topographies of varying spatial resolution are obtained by manipulating BedMachine Antarctica data. We compare model outputs obtained with the original dataset [6], which has a 500 m spatial resolution, to simulations initiated with a high- and low-resolution variation of the original dataset. We reduce BedMachine data to a 5 km spatial resolution to generate the low-resolution variation simply by subsampling the original dataset. To generate a high-resolution dataset, we first interpolate between data points to a grid with 100 m spacing using a cubic interpolation function. Then, to incorporate additional roughness that might be resolved from high-resolution bed topography data, we add randomly generated noise to the interpolated data sampled from a normal distribution centred at 0 m and with a standard deviation of 50 m, which we choose based on the accuracy of the original dataset. The mass conservation method used to interpolate ice thickness in BedMachine has a vertical accuracy of 30–60 m; however, local errors greater than 200 m may be present in poorly constrained regions where limited topography data are available [6]. The noise added to our interpolated high-resolution bed topography is within ±100 m for 95% of data points, which is reasonable.

In this synthetic high-resolution bed topography data, we mask the non-interpolated points, adding no additional noise to the points corresponding to the original dataset. As such, if we were to subsample the generated 100 m resolution bed data to a 500 m resolution at the correct x–y coordinates, we would obtain the original bed topography dataset from BedMachine precisely. The model domain and mesh are equivalent for all model simulations, so the variation in bed topography seen by the model is specifically due to the interpolation of datasets with different resolution.

(c) Subglacial hydrology modelling

We model the steady-state subglacial hydrological system for each of the three bed topographies using the GlaDS model [65]. GlaDS calculates the flow of water through the basal environment based on the hydraulic potential gradient, incorporating both distributed and channelized subglacial water flow. We set a zero-flux boundary condition along the edges of the model domain. The outflow boundary for the subglacial hydrology model is at the grounding line, where we define the hydraulic potential to be zero under the assumption of hydrostatic equilibrium of the ice shelf [26]. We run GlaDS until convergence criteria are met for both the subglacial water depth (Δh $< 10^{-6}$ m for 99% of nodes between three-month saved outputs) and the channelized discharge (ΔS $<10^{-5}$ m^3 s^{-1}). These conditions are met for all three simulations by model year 100. We choose a channel conductivity of 10^{-3} $m^{7/4}$ $kg^{-1/2}$ and a sheet conductivity of 5.0×10^{-2} $m^{3/2}$ $kg^{-1/2}$ [55,66]. Steady-state simulations are run for each of the three bed topographies using an adaptive time step determined by the Courant–Friedrichs–Lewy condition, which is calculated for subglacial hydrology based on the minimum time required for basal water to flow through any element in the domain, and ranges between 45 min early on in the simulation to more than 6 h once steady state is reached.

Synchronous coupling between subglacial hydrology and ice dynamics is utilized for three of our nine projections of Thwaites Glacier evolution, wherein both subglacial hydrology and ice dynamics freely evolve throughout the 285 year transient simulations. In this modelling framework, coupling occurs via basal friction as the dynamic link between the different physical mechanisms. GlaDS, initialized with ice velocity and geometry, calculates effective pressure from the distribution of water throughout the distributed and channelized hydraulic systems (see Werder *et al*. [65] for full model description). Effective pressure is used in the Schoof friction law to calculate basal shear stress, τ_b, which is then applied in the stress balance equations to calculate new ice geometry and velocity. These updated fields are fed back to GlaDS, which computes changes to the distribution of water within the subglacial environment and resulting effective pressure based on the evolving ice dynamics. We currently run all modules at a 6 h time step during transient simulations. In this coupling framework, we ignore changes to basal melt below grounded ice, which remains constant throughout our simulations. For projections using the coupled model framework, the outflow location becomes a moving boundary and is automatically updated as the ice geometry evolves and the grounding line retreats. A hydraulic potential of zero is imposed for all floating ice, and below grounded ice, the hydraulic potential freely evolves, driven by changes in the ice geometry and velocity.

A full list of model parameters utilized in the subglacial hydrology simulations can be viewed in electronic supplementary material, table S1.

(d) Model relaxation and transient runs

We initialize models with six parameter combinations by combining results obtained from the set of parallel inversion and thermal model steps corresponding to the initial two effective pressure representations with our three bed topography resolutions. The new effective pressure fields generated by the steady-state subglacial hydrology simulations using each of the bed topographies replace the initial modelled effective pressure field. The ice front defined by the BedMachine dataset is held constant across all model simulations, and we do not utilize a calving model. Furthermore, a minimum ice thickness of 25 m is imposed across the full model domain in the stress balance equations, and we assume that ice at this threshold is contributing little to the dynamics of the glacier. These choices help to stabilize the coupled model framework. GlaDS can become numerically unstable below thin ice, but imposing a minimum ice thickness for grounded ice can help to avoid convergence issues. Preliminary tests showed that even with a minimum thickness established, the introduction of a calving law in the coupled model quickly destabilizes GlaDS.

Thickness-driven calving laws applied in Antarctica often use a threshold value of 50 m or greater [67,68]. We mask ice that is not more than 25 m thick when plotting model results in figures.

We now run six sets of model relaxations for 15 years under constant climate conditions corresponding to the year 2015 of our forcing data to obtain the final set of initial conditions. All simulations lose mass during model relaxations owing to some grounding line retreat and thinning. Average rates of mass loss during the model relaxations range from 75 to 120 Gt a^{-1}. Thwaites and the surrounding region have experienced accelerated ice loss in the twenty-first century, with a range of values reported for the mass balance of Thwaites in 2015 calculated from satellite observations. An annual mass balance of -70 ± 19.4 Gt a^{-1} for the 2013–2017 time period was calculated using the gravimetric mass balance data product [69] for the Thwaites sector of Antarctica (Antarctic Ice Sheet basin 21 [70]), which is consistent with our modelling domain. Following relaxation, our models lose mass at a somewhat faster rate with the 5 km bed resolution models on the high end of that range. We find this to be a reasonable fit to observations. Final model outputs of ice velocity, geometry and pressure from the relaxations are used to initialize the transient simulations for the future ice evolution of Thwaites. At this point, we turn on the coupling mechanism between subglacial hydrology and ice dynamics for an additional three simulations, totalling nine model projections. These runs have the same initial conditions as those using a constant effective pressure modelled by GlaDS.

3. Results

(a) Steady-state subglacial hydrology

The steady-state subglacial hydrology results show several subglacial lakes below the main trunk of Thwaites for all three bed variations (figure 2d–f). These reach a maximum water depth of approximately 40 m but are generally on the order of 10 m deep. Maximum water depth varies with bed topography. The largest lakes present in all three models correspond with the locations of active subglacial lakes below Thwaites inferred from CryoSat-2 altimetry data [41]. We find that the high-resolution bed topography produces deeper subglacial lakes than the low-resolution bed, with maximum basal water depths of 39.2, 34.2 and 32.8 m for the 100 m, 500 m and 5 km bed resolutions, respectively. In addition, results using the high-resolution bed topography show some small subglacial lakes that are not present in the simulation that uses the low-resolution topography (figure 2d,f). These smaller lakes generally correspond with the locations of additional subglacial lakes below Thwaites recently identified by re-evaluation of radar altimeter data from satellite observations [42]. While the emergence of additional subglacial lakes in our model simulation using the high-resolution topography may be an artefact of resampling the bed, it is encouraging that the results are generally consistent with observations.

There is one large subglacial channel modelled in the domain, located below the fastest portion of the glacier (figure 2a–c). The shape and location of the channel are consistent across all three bed resolutions. However, we see significantly more small branches feeding into the main channel with the higher bed resolution. The magnitude of channelized discharge is only 44 $m^3\ s^{-1}$ in this higher-resolution run compared with the steady-state simulation with low-resolution bed topography, where we find that the maximum channelized discharge near the grounding line is nearly 70 $m^3\ s^{-1}$. Generally, we see fewer channel segments forming with lower bed resolution, but those that do form are larger.

(b) Sea-level rise projections

Each of our model simulations results in projected mass loss of Thwaites Glacier over the coming centuries, ranging from 45.5 to 102.8 mm of sea-level equivalent (SLE) by the year 2300 (table 1). The high-resolution coupled model (Bed_100 m-N_coupled) produces the largest projected sea-level rise from Thwaites across all model simulations. The smallest mass loss across all model

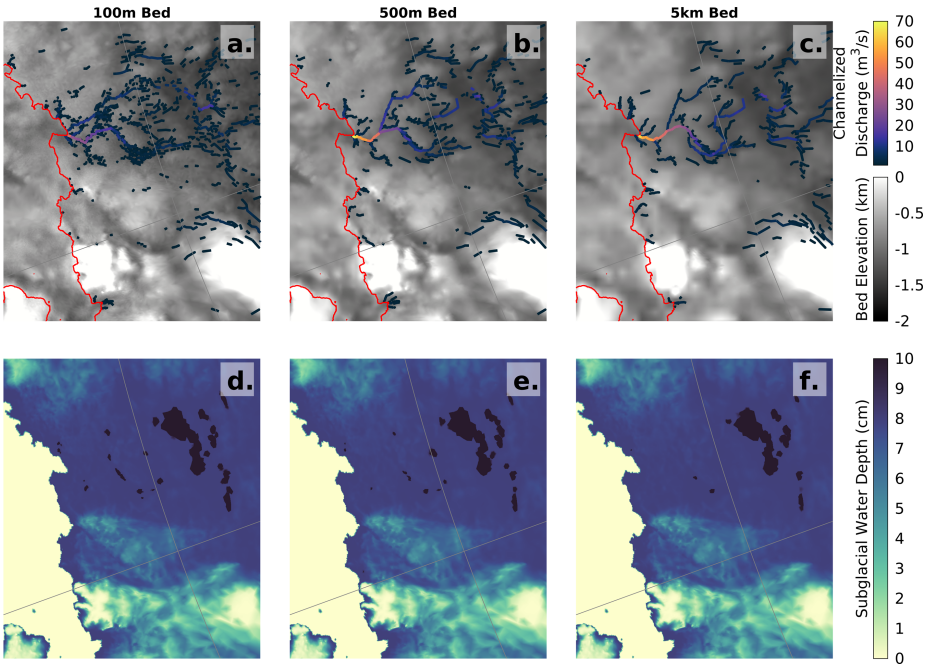

Figure 2. (a–c) Steady-state results from the subglacial hydrology model GlaDS [65] for the freshwater discharge flux in the channelized component of the hydrological system overlain on bed topography elevation. Channelized discharge less than 1 $m^3\ s^{-1}$ is not displayed. (d–f) Steady-state basal water thickness modelled by GlaDS. Water depths are limited to 10 cm in the colour map to display the spatial variation of water in the distributed system. Subglacial lakes appear as black outlines.

Table 1. Accumulated projected mass loss of Thwaites Glacier between 2015 and 2300 in SLE (mm) modelled using varying resolution of bed topography data and three different representations of effective pressure. All modelled effective pressure fields (*N*) are obtained from the subglacial hydrology model GlaDS.

simulation label	bed topography resolution	representation of effective pressure	projected sea-level rise (mm)
Bed_100 m-N_POC	100 m	constant *N*, POC	83.24
Bed_100 m-N_modelled	100 m	constant *N*, modelled	87.78
Bed_100 m-N_coupled	100 m	evolving *N*, modelled	102.78
Bed_500 m-N_POC	500 m	constant *N*, POC	45.52
Bed_500 m-N_modelled	500 m	constant *N*, modelled	45.75
Bed_500 m-N_coupled	500 m	evolving *N*, modelled	62.51
Bed_5 km-N_POC	5 km	constant *N*, POC	64.25
Bed_5 km-N_modelled	5 km	constant *N*, modelled	65.30
Bed_5 km-N_coupled	5 km	evolving *N*, modelled	88.62

simulations is from the original BedMachine dataset with constant effective pressure calculated from the assumption of POC (Bed_500 m-N_POC). However, the GlaDS constant (non-coupled) *N* simulation using this bed resolution (Bed_500 m-N_modelled) produces only 0.25 mm more mass loss in SLE. These two simulations are nearly identical throughout the model runs with respect to both timing and magnitude of mass loss (figure 3).

The model simulation with the third smallest mass loss of 62.5 mm SLE is the coupled model using the original BedMachine topography (Bed_500 m-N_coupled). At this bed resolution, using a time-evolving effective pressure that dynamically responds to changes in ice geometry produces a 36.6% increase in projected sea-level rise by the year 2300 as compared to using a constant effective pressure modelled by GlaDS. Including coupled effective pressure between the subglacial hydrology and ice dynamics model results in a larger degree of mass loss for all three bed topographies. We find a 17.1 and 35.7% increase in final projected mass loss caused by coupling effective pressure for simulations using a 100 m and 5 km bed resolution, respectively.

Initially, simulations using lower-resolution bed topography showed more mass loss than those using a higher resolution. During the first half of the simulation runtime, all three models using the 5 km bed produce more sea-level rise than either those using the 500 m or 100 m beds (figure 3a). In the model year 2150, the two low-resolution models with constant effective pressure (Bed_5 km-N_POC and Bed_5 km-N_modelled) seem to temporarily stabilize for approximately 50 years, while the coupled model (Bed_5 km-N_coupled) continues to lose mass (figure 3b). At the same time, all three low bed resolution simulations begin losing mass at an accelerated rate. In the year 2175 (approximately), all three high-resolution simulations surpass the two constant N low-resolution simulations. By the year 2300, the coupled high-resolution simulation results show the most mass loss (Bed_100 m-N_coupled), and the constant effective pressure runs (Bed_100 m-N_POC and Bed_100 m-N_modelled) have nearly caught up to the coupled low-resolution (Bed _5 km-N_coupled) simulation, which had been the fastest to lose mass initially.

(c) Grounding line retreat

An extensive grounding line retreat occurs in all nine simulations. However, the timing of the retreat and the final extent of retreat both vary depending on the combination of bed resolution and effective pressure representation.

Figure 4 shows grounding line retreat as periodic snapshots throughout each of the simulations, both spatially, as shown by the maps in panels (d–l), and as a one-dimensional distance along a central flowline in the fastest flowing portion of Thwaites, shown directly below each corresponding map. Ice geometries along the same flowline (see figure 1) are shown as profiles for each bed topography (figure 4a–c) above the corresponding simulations. By examining the diamond markers indicating the grounding line location along the flowline in various model years, indicated by colour, some trends emerge. Initially, in all model simulations, the grounding line does not retreat rapidly at the location of this particular flowline. We see clustering of the red, black, yellow and green diamonds in many of the line plots, indicating a locally stable grounding line or relatively slow retreat between the model years 2015 to 2150. For simulations using a 100 m bed resolution (figure 3d,g,j), these diamond markers are essentially overlapping, indicating that the grounding line does not significantly retreat at the location where the flowline was drawn until after year 2150, regardless of the choice of effective pressure representation. Examining the maps, we can see that there are portions of the grounding line that do begin to retreat prior to the year 2150, but large sections of these grounding lines overlap with one another. Once we examine the flowline retreat rate more closely, we see that decreasing the bed resolution causes increased spread in the red, black, yellow and green diamonds when comparing along rows, indicating a relatively faster retreat (e.g. figure 3d–f). In the first half of the model run time, until year 2150, we have faster grounding line retreat with smoother bed topographies.

Examining the pink and blue diamond markers, we start to see large-scale and rapid retreat occurring at different time periods. For example, the blue diamond is in a relatively similar position for panels (d) and (g) in figure 3, indicating that by year 2250, retreat to a similar position has been reached in these two simulations. This can also be seen spatially in the maps. However, examining the pink diamond, corresponding to the year 2200, we see that in panel (g), it is approximately 90 m along the flowline, while it is still at approximately 80 m in panel (d). This shows that although both simulations are undergoing rapid retreat, the retreat rates are not the same

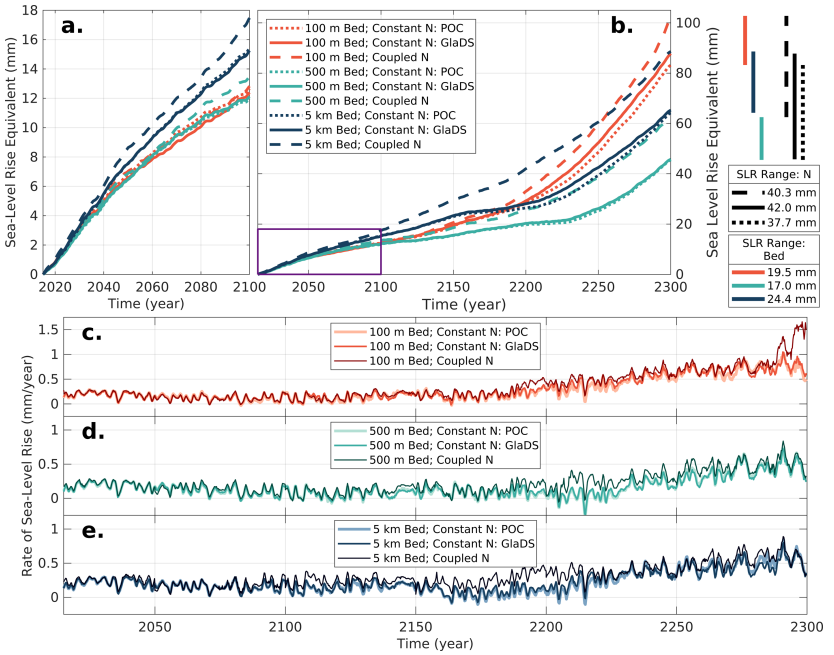

Figure 3. Projected sea-level rise of Thwaites Glacier from 2015 until the year (a) 2100 and (b) 2300 for nine model simulations using various combinations of bed topography resolution and representation of effective pressure, *N*. The bars to the right of the *y*-axis in (b) indicate the final range in sea-level rise grouped by bed resolution (coloured bars) and effective pressure (black bars). Rate of sea-level rise (c–e) for each of the bed topography resolutions.

and they are not constant. We also see that the coupled model with high bed resolution (panel (j)) is now retreating much faster than either simulation that uses a constant effective pressure field by year 2250 (panels (d) and (g)).

The onset of rapid grounding line retreat appears to be around the year 2200 for most simulations. The pink grounding line is visibly retreated inland across a large portion of the domain shown for each simulation. The notable exception to this is the coupled model using the low-resolution bed (Bed_5 km-N_coupled; panel (l)), which displays extensive retreat by year 2150 (green line).

(d) Changes in ice velocity and glacier geometry

All nine projections of Thwaites show ice acceleration by the end of the model simulations (figure 5). We see velocity increases that exceed 2 km a^{-1} in every simulation, with some reaching 4 km a^{-1}. The most dramatic acceleration occurs for the simulations using a high bed resolution and coupled effective pressure (Bed_100 m-N_coupled; panel (g)). Ice velocity increases much farther inland for this simulation than for all others. We see a similar pattern in total ice thinning across the model results as with ice acceleration (electronic supplementary material, fig. S9). One simulation (Bed_100 m-N_coupled; panel (g)) shows extensive thinning that exceeds 500 m over a comparatively large portion of the model domain. Focusing on the portion of the map just to the left of the 76°S latitude line, we can see that large-scale ice thinning extends farther inland for all three model simulations using the high-resolution bed topography (column one) than for either the 500 m bed resolution (column two) or the 5 km bed resolution (column three).

We do not allow the ice shelf extent to change in our model simulations, as discussed in §2. All simulations show extensive thinning of the ice shelf, which is allowed to reach a minimum thickness of 25 m. Assuming that ice this thin does not substantially affect glacier dynamics and

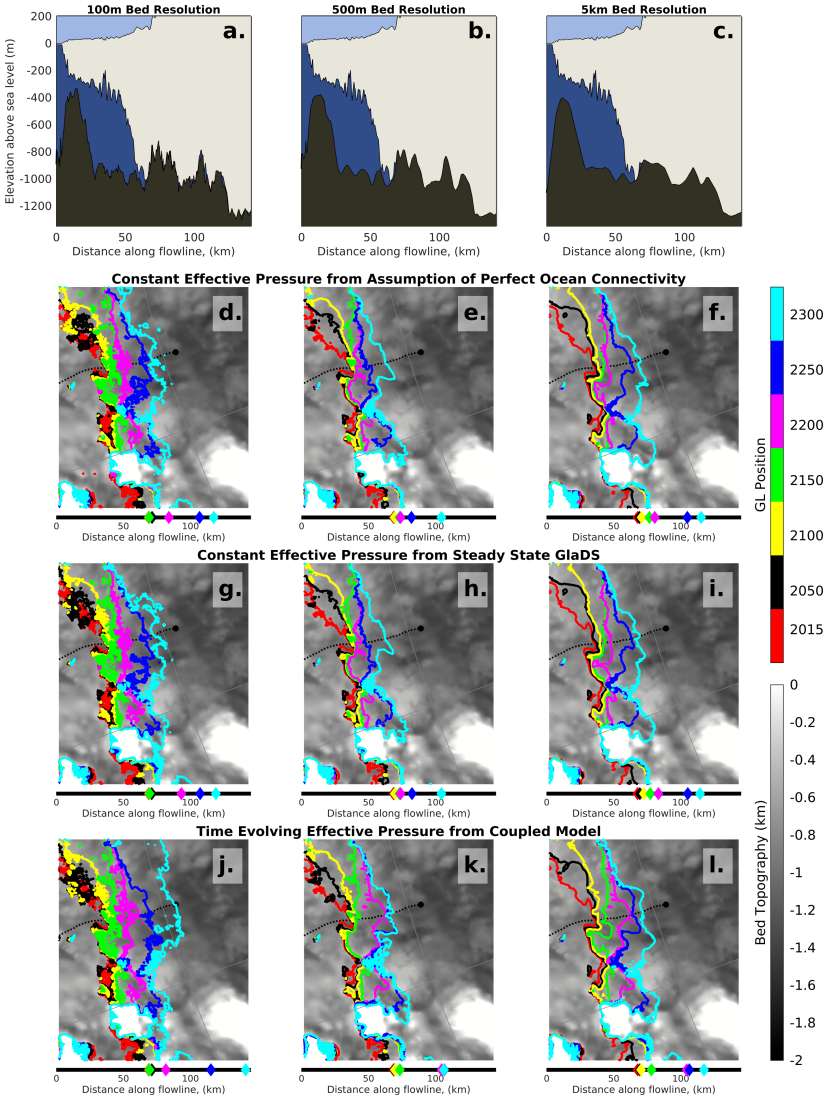

Figure 4. Profiles of initial ice geometries for three bed topographies used in model experiments: (a) 100 m, (b) 500 m and (c) 5 km resolution. (d–l) Modelled grounding line location at various snapshots in time throughout each simulation. Directly below the map in each panel is a one-dimensional plot showing the grounding line location along the flowline shown in map panels (dashed black line). The location of the flowline with respect to the larger model domain can be seen in figure 4*b*. The 500 m bed is the unaltered BedMachine topography [6] and is used as the background plot in maps shown in d–l.

would typically calve off using most, if not all, calving laws, we take the ice thickness threshold of 25 m to be a proxy for the new ice front. Ice, 25 m thick, is masked out in figure 5 and electronic supplementary material, fig. S9, which allows for the approximate ice front in the year 2300 to be visible. The final ice extent is similar across all bed topographies for simulations using constant effective pressure (figure 5a–f and electronic supplementary material, fig. S9*a–f*). Small differences in the shape of the ice front are visible in these simulations, but the location of the new ice extent is very similar. This is particularly prominent in electronic supplementary material, fig. S9. Notably, these six simulations effectively no longer have an ice shelf in 2300. This is not true for the coupled model simulations (figure 5g–i and electronic supplementary material, fig. S9*g–i*). In these three simulations, the final ice extent is further extended, and a floating shelf is still present in front of the main trunk of Thwaites Glacier.

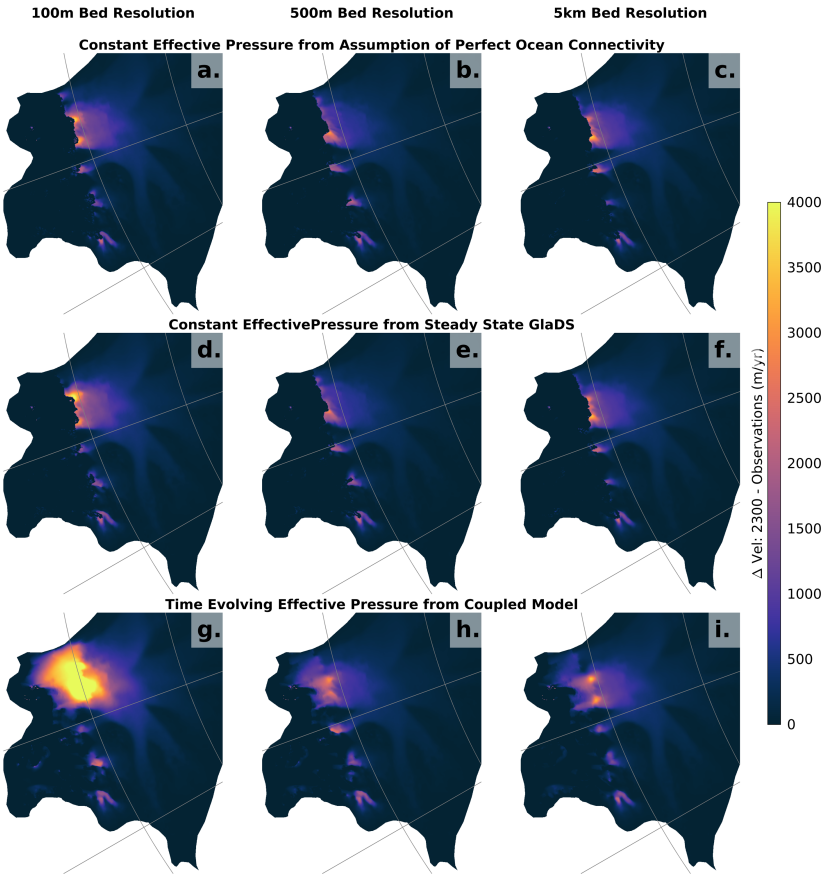

Figure 5. Change in ice velocity (m a^{-1}) at the end of each simulation in model year 2300 as compared to satellite observations of surface velocity [33]. Bed resolution is identified for each column and subglacial hydrology representation is identified for each row.

4. Discussion

(a) Bed topography

Bed topography is highly influential in determining how the subglacial hydrological system evolves. Additional bed roughness represented in the higher-resolution topography results in more water remaining in the distributed component of the system, as seen in the steady-state GlaDS simulations (figure 2). Smoother bed topography seems to promote channelization, perhaps from decreasing the number of depressions that can trap basal water and removing obstacles around which water has to flow. Our ability to understand the processes occurring in the basal environment necessarily depends on the use of models owing to the limited ability to collect direct measurements of the system and the difficulty associated with properly representing subglacial systems in laboratories. However, model results are sensitive to input data, as we show here. The impact that subglacial hydrology has on glacier flow is a key component of ice dynamics that is largely missing from our understanding of these systems [71]. To properly address this knowledge gap and ultimately improve the accuracy of sea-level rise projections, we need high-resolution bed data spanning the fast-flowing region of all the major ice streams and coupled hydrology and ice dynamic modelling.

Our model results suggest that bed topography exerts a high degree of control on glacier evolution and is more effective on total mass loss than the representation of effective pressure

when these variables are considered independently. This can be clearly seen by examining the coloured bars adjacent to the *y*-axis in figure 3. Although one low bed resolution model (Bed_5 km-N_coupled) projects a particularly high degree of mass loss, the results are generally clustered based on the bed resolution utilized, with all three models using the 100 m generated bed topography resulting in more than 80 mm of sea-level rise. However, there is a compounding effect between bed topography and time-evolving effective pressure. Each effective pressure produces simulations with a large overlapping range of resulting mass loss, as seen by the black bars adjacent to figure 3b. Within our experiments, the choice of effective pressure representation alone does not determine the magnitude of mass loss. However, given a specific bed topography, the coupled model results in a significantly larger ice volume change than either constant effective pressure field. This illustrates the importance of considering the transient evolution of basal water in projections of future sea-level rise.

Comparing the ice geometry profiles (figure 4a–c), we can see an elevated portion of the bed, 75 km along the flowline, where the grounding line is initially stabilized. This region is lowered by approximately 100 m in the 5 km bed resolution data (figure 4c), creating a smooth plateau-like feature in place of the ridge present in the other datasets. In the profiles of the 100 and 500 m bed, this elevated region seems to initially slow down grounding line retreat past this ridge and into deeper portions of the subglacial basin. Two additional elevated portions of the bed are visible along this particular flowline at approximately 105 and 120 m along the profile, which seem to act as pinning points by temporarily stabilizing the grounding line. Eventually, the magnitude of ocean thermal forcing initiates rapid grounding line retreat in each simulation, and the ocean warming seems to dominate over all other dynamics at play. This is consistent with results from other modelling studies. Seroussi *et al*. [58] found large variability in the timing of retreat initiation for the Antarctic Ice Sheet among an ISMIP6 model ensemble. However, once initiated, they found a highly consistent retreat rate across individual model simulations. Among this ensemble, retreat under high-emissions scenarios for Thwaites is initiated in the year 2100 or 2200, depending on the specific scenario, with a retreat rate of 3.5 km a^{-1}. The authors conclude that the consistent retreat rate across ice-sheet models indicates that during phases of fast retreat, retreat rate is determined by bed topography as opposed to particular model physics. In our results, we see steeper slopes in accumulated sea-level rise during the last 100 years of the simulations for the 100 m bed topography (pink curves in figure 2b) compared with the other bed resolutions, which is consistent with this conclusion.

The magnitude of total mass loss seems dependent on the specific bed topography, although not necessarily on the bed resolution. Although the high-resolution bed resulted in the largest volume of mass loss, the magnitude of mass loss is not ordered by increasing bed resolution. Results from the low-resolution bed topography showed more sea-level rise than the results obtained from the original BedMachine dataset. This indicates that it is important to not only consider the resolution of the bed data but also the specific realization of the bed represented in the model, as small-scale differences in topography can produce a model that is significantly more sensitive to climate forcing. Differences between the 100 and 500 m resolution topographies may actually be the result of resampling the data rather than from altering the spatial resolution. To properly tease apart the effect of bed resolution versus the specific realization, it is necessary to run a much larger ensemble of models. By generating multiple high-resolution bed topographies with statistically consistent roughness and sampling these variations at different low resolutions, it would be possible to definitively address the effect of using high-resolution bed topography in ice-sheet models. Does the high-resolution bed always retreat at a more rapid rate once retreat is initiated, or is that specific to this realization of the bed topography? Is there a threshold resolution at which high-resolution data do not result in significant differences in modelled ice flow? A large model ensemble was outside the scope of this work, but our results indicate that the relationship between modelled ice flow and bed resolution is not straightforward, and a large-scale investigation of the effects of small-scale variation in bed topography would be informative.

Ice-sheet projections beyond the year 2100 often use climate forcing from SSP 1-2.6 and 5-8.5 as representative low- and high-emissions scenarios [72–74]. Some studies have included projections under mid-emissions scenarios [75–77], but these have not been common enough in the literature to be included for assessment in the IPCC Sixth Assessment Report [78]. In cases where the goal is to improve our understanding of ice-sheet physics, the relative importance of different physical mechanisms, or to specific parameter choices, it would be highly beneficial to also utilize moderate emissions scenarios where ocean warming does not reach such large magnitudes as to induce rapid retreat and mass loss ubiquitously. It is useful and important to run high-emissions scenarios in ice-sheet models, as these are more likely to show us where critical temperature thresholds are for different glaciers [79]. But it is unsurprising that high-emissions scenarios with large degrees of ocean warming typically result in extensive retreat and mass loss regardless of other factors. Results obtained using a smaller degree of ocean thermal forcing may highlight effects coming from differences in modelling choices, such as parameter values, included physics and input data, as it is unlikely that models initiated in different ways would be equally sensitive to smaller perturbations in forcing.

(b) Variations of constant effective pressure

Our results do not show a meaningful difference when using the steady-state effective pressure modelled by GlaDS versus the standard approximation based on ice and bed geometries alone. However, this is inconsistent with results from a recent study that found subglacial water amplifies Antarctic sea-level rise [80]. The authors used multiple methods to represent basal water, including a steady-state N modelled by GlaDS and N calculated under the assumption of POC, as we utilize here. They found that using these representations of effective pressure in sea-level rise projections produced different degrees of mass loss, with the POC representation yielding approximately 30 cm more sea-level rise than steady-state GlaDS across the full Antarctic Ice Sheet by year 2300. Several factors may explain why our model is less sensitive to spatial variation in the effective pressure field when this variable is held constant in time. Here, we are only looking at one drainage basin, and it is possible that the specific geometry of Thwaites is such that the differences between N_POC and N_modelled are not critical in determining the evolution of the glacier under this particular warming scenario. We also use a relatively high Iken bound, $C_{\max}$= 0.8 [81], in the Schoof friction law, which affects the model's sensitivity to regions of low effective pressure, in particular. The accepted range C_{max} is 0.17–0.84 [54], and it is generally used as a tuning parameter in the friction inversion within this range. The Iken bound is the ratio of basal shear stress to effective pressure, τ_b/N, and acts as a limit on τ_b in the Coulomb sliding regime where effective pressure is generally low. In fast-flowing regions with low effective pressure, $\tau_b \sim C_{\max}N$, while in the Weertman sliding regime, $\tau_b \sim Cu_b^m$, where C is the inverted coefficient in the Schoof friction law, u_b is the sliding velocity and m is the exponent used in the friction law [14,47,82].

In an analysis of sensitivity to friction law parameters, Kazmierczak *et al*. [30] found that subglacial hydrology modulates basal sliding, such that lower effective pressure near the grounding line resulted in a higher sensitivity to climate forcing. The authors found that compared with simulations that fully excluded effective pressure, including some representation of subglacial hydrology, resulted in increased mass loss. Different representations of subglacial hydrology also affected the total sea-level contribution. These simulations were all conducted using the Weertman–Budd friction law. Although we do not find a notable difference in the POC approximation versus effective pressure from steady-state GlaDS in this particular model of Thwaites, sensitivity to the parametrization method for effective pressure may be more significant for some friction laws [30] or given different parameter choices [80]. Despite being an important component of ice-sheet dynamics, there is still much that remains poorly understood with respect to how to properly represent basal friction in models, leaving many choices regarding how to specifically parametrize the physics of the basal environment up to the modeller's discretion. This remains an active area of research.

(c) Coupling subglacial hydrology and ice dynamics in sea-level rise projections

The model simulation that resulted in the largest total mass loss was the coupled model with the high-resolution bed topography (table 1; Bed_100 m-N_coupled). In this simulation, we see extensive grounding line retreat (figure 4*j*) and ice thinning exceeding 500 m over a large portion of the model domain (electronic supplementary material, fig. S9*g*). This simulation also shows the largest increase in ice velocity, speeding up by more than 4 km a^{-1} by the year 2300 (figure 5g). It is not clear whether all the simulations would reach this degree of retreat, acceleration and thinning if the model time were to extend beyond the year 2300 or if the coupled model framework is inherently less stable beyond some threshold in climate forcing. Evidence towards the former can be found by comparing row three to rows one and two in figure 5. When we look at the region and magnitude of ice acceleration, we see that, although the changes seem more pronounced in the coupled model simulations, they are comparable to the changes in the 100 m bed resolution simulation using constant modelled effective pressure (figure 5d). This seems to indicate that the coupled model framework simply responds faster to large perturbations in atmospheric and ocean forcing than when a constant effective pressure is used due to a compounding effect of higher sensitivity of the coupled model and of the high-resolution bed topography.

In our coupled model framework, we neglect several key connections where subglacial hydrology and ice dynamics interact in important ways. Here, we only consider the relationship between basal water pressure and sliding velocity as represented through the effective pressure term in the friction law. We do not allow for the water source term in GlaDS to change during simulations, although the frictional melting of basal ice necessarily changes when the sliding velocity changes. Additional basal melting induced by faster sliding speeds would increase the volume of water distributed throughout the subglacial hydrologic system. In regions where basal water pressure is less than ice overburden pressure, this will decrease effective pressure and result in faster sliding speeds and further enhanced basal melting as a result. However, increased basal water pressure in regions where water pressure is already close in magnitude to ice pressure will probably promote channelization, reducing effective pressure by removing water from the basal environment efficiently and ultimately limiting the velocity response. The balance between these contending processes remains largely unexplored, but is important to consider, especially given the large magnitude of ice acceleration found in our results.

We additionally neglect the effect of subglacial discharge on ice shelf melting, with our ocean-driven melt parametrization dependent upon far-field ocean temperature and salinity alone. However, subglacial discharge has long been cited as a probable critical factor in accurately calculating ice shelf melt rates and in determining long-term ice shelf stability [83–85]. It has been shown that many ice shelf channels are initiated at locations where models have predicted subglacial discharge [86], and that regions where freshwater flow from the subglacial environment crosses the grounding line are characterized by enhanced sub-ice shelf melt [21,87]. Subglacial discharge has also been shown to increase modelled ice shelf melt rates near the grounding line, producing a better match to estimates calculated from satellite observations [88,89], and recent studies have shown that when subglacial discharge is included in ice shelf melt calculations in projections of future glacier evolution, the onset of retreat is accelerated [18,81]. This indicates that the freshwater flux from the subglacial environment is an important variable to consider with regard to glacier destabilization under a warming climate. However, the ability to couple subglacial hydrology and ice flow models is still a somewhat recent development, and fully integrating the models into a synchronously coupled system that represents all the major dynamic links still requires additional work.

5. Conclusion

Here, we present modelled evolution of Thwaites Glacier with different bed topography and subglacial hydrology parametrizations until the year 2300. We find that under moderate ocean

forcing, lower-resolution bed topography results in more extensive grounding line retreat. However, after the year 2150, when the ocean temperature begins to increase rapidly, the retreat rate of simulations using the high-resolution bed topography increases, producing some of the largest projections of sea-level rise by the year 2300. Overall, extensive retreat is visible across all parameter combinations and model frameworks examined here, indicating that, under large enough thermal forcing from the ocean, extensive retreat and mass loss will occur regardless of variation in model initialization or the inclusion of secondary physical mechanisms. In addition, our results show that including time-evolving effective pressure from coupling subglacial hydrology and ice dynamics increases projected sea-level rise. It is therefore likely that model projections ignoring subglacial hydrology underestimate sea-level rise. As models further improve their capacity to fully couple these systems, it is likely that sea-level projections will further increase beyond what we find in these experiments. Extensive bed topography data determine our ability to model glaciers and ice sheets accurately, and bed topography is highly influential for all components of glacier modelling. We find that even small-scale variations in topography can cause large deviations in resulting glacier evolution and subsequent sea-level rise. As ice-sheet models incorporate improved physics and finer grid spacing, the need for high-resolution bed data continues to be an essential input and key factor in determining modelled behaviour.

Data accessibility. Data are available on Dryad [90]. Supplementary material is available online [91].

Declaration of AI use. We have not used AI-assisted technologies in creating this article.

Authors' contributions. S.E.: conceptualization, data curation, formal analysis, methodology, visualization, writing—original draft; C.D.: conceptualization, funding acquisition, project administration, resources, supervision, writing—review and editing.

Both authors gave final approval for publication and agreed to be held accountable for the work performed therein.

Conflict of interest declaration. We declare we have no competing interests.

Funding. This work was performed with support by the Natural Sciences and Engineering Research Council of Canada (NSERC RGPIN-03761-2017) and C.D. was also supported by the Canada Research Chairs Program (CRC 950-231237).

Acknowledgements. The authors would like to thank the Digital Research Alliance of Canada for access to supercomputing resources.

References

1. Greenwood SL, Simkins LM, Winsborrow MCM, Bjarnadóttir LR. 2021 Exceptions to bed-controlled ice sheet flow and retreat from glaciated continental margins worldwide. *Sci. Adv.* **7**, eabb6291. (doi:10.1126/sciadv.abb6291)
2. Winsborrow MCM, Clark CD, Stokes CR. 2010 What controls the location of ice streams? *Earth Sci. Rev.* **103**, 45–59. (doi:10.1016/j.earscirev.2010.07.003)
3. Katz RF, Worster MG. 2010 Stability of ice-sheet grounding lines. *Proc. R. Soc. A Math. Phys. Eng. Sci.* **466**, 1597–1620. (doi:10.1098/rspa.2009.0434)
4. Robel AA, Schoof C, Tziperman E. 2016 Persistence and variability of ice-stream grounding lines on retrograde bed slopes. *Cryosphere* **10**, 1883–1896. (doi:10.5194/tc-10-1883-2016)
5. Bingham RG *et al*. 2017 Diverse landscapes beneath Pine Island Glacier influence ice flow. *Nat. Commun.* **8**, 1618. (doi:10.1038/s41467-017-01597-y)
6. Morlighem M *et al*. 2020 Deep glacial troughs and stabilizing ridges unveiled beneath the margins of the Antarctic ice sheet. *Nat. Geosci.* **13**, 132–137. (doi:10.1038/s41561-019-0510-8)
7. Pritchard HD *et al*. 2025 Bedmap3 updated ice bed, surface and thickness gridded datasets for Antarctica. *Sci. Data* **12**, 414. (doi:10.1038/s41597-025-04672-y)
8. Berger S, Favier L, Drews R, Derwael JJ, Pattyn F. 2016 The control of an uncharted pinning point on the flow of an Antarctic ice shelf. *J. Glaciol.* **62**, 37–45. (doi:10.1017/jog.2016.7)
9. Durand G, Gagliardini O, de Fleurian B, Zwinger T, Le Meur E. 2009 Marine ice sheet dynamics: hysteresis and neutral equilibrium. *J. Geophys. Res. Earth Surf.* **114**, F001170. (doi:10.1029/2008JF001170)

10. Weertman J. 1974 Stability of the junction of an ice sheet and an ice shelf. *J. Glaciol*. **13**, 3–11. (doi:10.1017/S0022143000023327)
11. Schoof C. 2007 Ice sheet grounding line dynamics: steady states, stability, and hysteresis. *J. Geophys. Res*. **112**, F000664. (doi:10.1029/2006jf000664)
12. Favier L, Pattyn F, Berger S, Drews R. 2016 Dynamic influence of pinning points on marine ice-sheet stability: a numerical study in Dronning Maud Land, East Antarctica. *Cryosphere* **10**, 2623–2635. (doi:10.5194/tc-10-2623-2016)
13. Smith AM, Murray T. 2009 Bedform topography and basal conditions beneath a fast-flowing West Antarctic ice stream. *Quat. Sci. Rev*. **28**, 584–596. (doi:10.1016/j.quascirev.2008.05.010)
14. Iken A. 1981 The effect of the subglacial water pressure on the sliding velocity of a glacier in an idealized numerical model. *J. Glaciol*. **27**, 407–421. (doi:10.1017/s0022143000011448)
15. Hewitt IJ, Schoof C, Werder MA. 2012 Flotation and free surface flow in a model for subglacial drainage. Part 2. Channel flow. *J. Fluid Mech*. **702**, 157–187. (doi:10.1017/jfm.2012.166)
16. Schoof C, Hewitt IJ, Werder MA. 2012 Flotation and free surface flow in a model for subglacial drainage. Part 1. Distributed drainage. *J. Fluid Mech*. **702**, 126–156. (doi:10.1017/jfm.2012.165)
17. Arnold N, Sharp M. 2002 Flow variability in the Scandinavian ice sheet: modelling the coupling between ice sheet flow and hydrology. *Quat. Sci. Rev*. **21**, 485–502. (doi:10.1016/s0277-3791(01)00059-2)
18. Pelle T, Greenbaum JS, Dow CF, Jenkins A, Morlighem M. 2023 Subglacial discharge accelerates future retreat of Denman and Scott Glaciers, East Antarctica. *Sci. Adv*. **9**, eadi9014. (doi:10.1126/sciadv.adi9014)
19. Robel AA, Wilson E, Seroussi H. 2022 Layered seawater intrusion and melt under grounded ice. *Cryosphere* **16**, 451–469. (doi:10.5194/tc-16-451-2022)
20. Dow CF, Werder MA, Nowicki S, Walker RT. 2016 Modeling Antarctic subglacial lake filling and drainage cycles. *Cryosphere* **10**, 1381–1393. (doi:10.5194/tc-10-1381-2016)
21. Dow CF, Ross N, Jeofry H, Siu K, Siegert MJ. 2022 Antarctic basal environment shaped by high-pressure flow through a subglacial river system. *Nat. Geosci*. **15**, 892–898. (doi:10.1038/s41561-022-01059-1)
22. Wearing MG, Dow CF, Goldberg DN, Gourmelen N, Hogg AE, Jakob L. 2024 Characterizing subglacial hydrology within the amery ice shelf catchment using numerical modeling and satellite altimetry. *J. Geophys. Res. Earth Surf*. **129**, e2023JF007421. (doi:10.1029/2023JF007421)
23. Joughin I, Shean DE, Smith BE, Dutrieux P. 2016 Grounding line variability and subglacial lake drainage on Pine Island Glacier, Antarctica. *Geophys. Res. Lett*. **43**, 9093–9102. (doi:10.1002/2016gl070259)
24. Fricker HA, Carter SP, Bell RE, Scambos T. 2014 Active lakes of recovery ice stream, East Antarctica: a bedrock-controlled subglacial hydrological system. *J. Glaciol*. **60**, 1015–1030. (doi:10.3189/2014jog14j063)
25. Brondex J, Gillet-Chaulet F, Gagliardini O. 2019 Sensitivity of centennial mass loss projections of the Amundsen basin to the friction law. *Cryosphere* **13**, 177–195. (doi:10.5194/tc-13-177-2019)
26. Cook SJ, Christoffersen P, Todd J, Slater D, Chauché N. 2020 Coupled modelling of subglacial hydrology and calving-front melting at Store Glacier, West Greenland. *The Cryosphere* **14**, 905–924. (doi:10.5194/tc-14-905-2020)
27. Cook S, Christoffersen P, Todd J. 2022 A fully-coupled 3D model of a large Greenlandic outlet glacier with evolving subglacial hydrology, frontal plume melting and calving. *J. Glaciol.* **68**, 486–502. (doi:10.1017/jog.2021.109)
28. Ehrenfeucht S, Morlighem M, Rignot E, Dow CF, Mouginot J. 2023 Seasonal acceleration of Petermann Glacier, Greenland, from changes in subglacial hydrology. *Geophys. Res. Lett*. **50**, e2022GL098009. (doi:10.1029/2022GL098009)
29. Khan SA, Morlighem M, Ehrenfeucht S, Seroussi H, Choi Y, Rignot E, Humbert A, Pickell D, Hassan J. 2024 Inland summer speedup at Zachariæ Isstrøm, Northeast Greenland, driven by subglacial hydrology. *Geophys. Res. Lett*. **51**, e2024GL110691. (doi:10.1029/2024GL110691)
30. Kazmierczak E, Sun S, Coulon V, Pattyn F. 2022 Subglacial hydrology modulates basal sliding response of the Antarctic ice sheet to climate forcing. *Cryosphere Discuss*. **2024**, 1–24. (doi:10.5194/tc-16-4537-2022)
31. McArthur K, McCormack FS, Dow CF. 2023 Basal conditions of Denman Glacier from glacier hydrology and ice dynamics modeling. *Cryosphere Discuss*. **2023**, 1–29. (doi:10.5194/tc-17-4705-2023)

32. Howat IM, Porter C, Smith BE, Noh MJ, Morin P. 2019 The reference elevation model of Antarctica. *Cryosphere* **13**, 665–674. (doi:10.5194/tc-13-665-2019)
33. Mouginot J, Rignot E, Scheuchl B. 2019 Continent-wide, interferometric SAR phase, mapping of Antarctic ice velocity. *Geophys. Res. Lett*. **46**, 9710–9718. (doi:10.1029/2019gl083826)
34. Alley KE *et al*. 2021 Two decades of dynamic change and progressive destabilization on the Thwaites Eastern Ice Shelf. *Cryosphere* **15**, 5187–5203. (doi:10.5194/tc-15-5187-2021)
35. Chartrand AM, Howat IM, Joughin IR, Smith BE. 2024 Thwaites Glacier thins and retreats fastest where ice-shelf channels intersect its grounding zone. *Cryosphere* **18**, 4971–4992. (doi:10.5194/tc-18-4971-2024)
36. Miles BWJ, Stokes CR, Jenkins A, Jordan JR, Jamieson SSR, Gudmundsson GH. 2020 Intermittent structural weakening and acceleration of the Thwaites Glacier Tongue between 2000 and 2018. *J. Glaciol*. **66**, 485–495. (doi:10.1017/jog.2020.20)
37. Mouginot J, Rignot E, Scheuchl B. 2014 Sustained increase in ice discharge from the Amundsen Sea Embayment, West Antarctica, from 1973 to 2013. *Geophys. Res. Lett*. **41**, 1576–1584. (doi:10.1002/2013gl059069)
38. Graham AGC *et al*. 2022 Rapid retreat of Thwaites Glacier in the pre-satellite era. *Nat. Geosci*. **15**, 706–713. (doi:10.1038/s41561-022-01019-9)
39. Rignot E, Mouginot J, Morlighem M, Seroussi H, Scheuchl B. 2014 Widespread, rapid grounding line retreat of Pine Island, Thwaites, Smith, and Kohler glaciers, West Antarctica, from 1992 to 2011. *Geophys. Res. Lett*. **41**, 3502–3509. (doi:10.1002/2014gl060140)
40. Feldmann J, Levermann A. 2015 Collapse of the West Antarctic Ice Sheet after local destabilization of the Amundsen Basin. *Proc. Natl Acad. Sci. USA* **112**, 14191–14196. (doi:10.1073/pnas.1512482112)
41. Smith BE, Gourmelen N, Huth A, Joughin I. 2017 Connected subglacial lake drainage beneath Thwaites Glacier, West Antarctica. *Cryosphere* **11**, 451–467. (doi:10.5194/tc-11-451-2017)
42. Kim BH, Lee CK, Seo KW, Lee WS, Park JW. 2025 New catalog of Thwaites glacier subglacial lakes and their activity revealed by CryoSat-2 altimetry. *J. Geophys. Res. Earth Surf*. **130**, e2023JF007602. (doi:10.1029/2023JF007602)
43. Gourmelen N, Jakob L, Holland PR, Dutrieux P, Goldberg D, Bevan S, Luckman A, Malczyk G. 2025 The influence of subglacial lake discharge on Thwaites Glacier ice-shelf melting and grounding-line retreat. *Nat. Commun*. **16**, 2272. (doi:10.1038/s41467-025-57417-1)
44. Larour E, Seroussi H, Morlighem M, Rignot E. 2012 Continental scale, high order, high spatial resolution, ice sheet modeling using the Ice Sheet System Model (ISSM). *J. Geophys. Res*. **117**, 1–20. (doi:10.1029/2011JF002140)
45. MacAyeal DR. 1989 Large-scale ice flow over a viscous basal sediment: theory and application to ice stream B, Antarctica. *J. Geophys. Res*. **94**, 4071–4087. (doi:10.1029/jb094ib04p04071)
46. Morlighem M, Seroussi H, Larour E, Rignot E. 2013 Inversion of basal friction in Antarctica using exact and incomplete adjoints of a higher-order model. *J. Geophys. Res*. **118**, 1746–1753. (doi:10.1002/jgrf.20125)
47. Schoof C. 2005 The effect of cavitation on glacier sliding. *Proc. R. Soc. A*. **461**, 609–627. (doi:10.1098/rspa.2004.1350)
48. Åkesson H, Morlighem M, Nilsson J, Stranne C, Jakobsson M. 2022 Petermann ice shelf may not recover after a future breakup. *Nat. Commun*. **13**, 2519. (doi:10.1038/s41467-022-29529-5)
49. Cheng G, Morlighem M, Mouginot J, Cheng D. 2022 Helheim Glacier's terminus position controls its seasonal and inter-annual ice flow variability. *Geophys. Res. Lett*. **49**, e2021GL097085. (doi:10.1029/2021GL097085)
50. Nias IJ, Nowicki S, Felikson D, Loomis B. 2023 Modeling the Greenland ice sheet's committed contribution to sea level during the 21st century. *J. Geophys. Res. Earth Surf*. **128**, e2022JF006914. (doi:10.1029/2022JF006914)
51. Schlegel NJ, Seroussi H, Schodlok MP, Larour EY, Boening C, Limonadi D, Watkins MM, Morlighem M, van den Broeke MR. 2018 Exploration of Antarctic Ice Sheet 100-year contribution to sea level rise and associated model uncertainties using the ISSM framework. *Cryosphere* **12**, 3511–3534. (doi:10.5194/tc-12-3511-2018)
52. Seroussi H, Morlighem M. 2018 Representation of basal melting at the grounding line in ice flow models. *Cryosphere* **12**, 3085–3096. (doi:10.5194/tc-12-3085-2018)

53. Wolovick M, Humbert A, Kleiner T, Rückamp M. 2023 Regularization and L-curves in ice sheet inverse models: a case study in the Filchner–Ronne catchment. *Cryosphere* **17**, 5027–5060. (doi:10.5194/tc-17-5027-2023)
54. Cuffey KM, Paterson WSB. 2010 *The physics of glaciers*, 4th edn. Oxford, UK: Elsevier.
55. Ehrenfeucht S, Dow C, McArthur K, Morlighem M, McCormack FS. 2025 Antarctic wide subglacial hydrology modeling. *Geophys. Res. Lett.* **52**, e2024GL111386. (doi:10.1029/2024GL111386)
56. Seroussi H, Morlighem M, Rignot E, Khazendar A, Larour E, Mouginot J. 2013 Dependence of century-scale projections of the Greenland ice sheet on its thermal regime. *J. Glaciol.* **59**, 1024–1034. (doi:10.3189/2013jog13j054)
57. Nowicki SMJ, Payne A, Larour E, Seroussi H, Goelzer H, Lipscomb W, Gregory J, Abe-Ouchi A, Shepherd A. 2016 Ice Sheet model intercomparison project (ISMIP6) contribution to CMIP6. *Geosci. Model Dev.* **9**, 4521–4545. (doi:10.5194/gmd-9-4521-2016)
58. Seroussi H *et al*. 2024 Evolution of the Antarctic ice sheet over the next three centuries From an ISMIP6 model ensemble. *Earths. Future* **12**, e2024EF004561. (doi:10.1029/2024EF004561)
59. Van Wessem JM *et al*. 2014 Improved representation of East Antarctic surface mass balance in a regional atmospheric climate model. *J. Glaciol.* **60**, 761–770. (doi:10.3189/2014JoG14J051)
60. Pelle T, Morlighem M, Bondzio JH. 2019 Brief communication: PICOP, a new ocean melt parameterization under ice shelves combining PICO and a plume model. *Cryosphere* **13**, 1043–1049. (doi:10.5194/tc-13-1043-2019)
61. Reese R, Albrecht T, Mengel M, Asay-Davis X, Winkelmann R. 2018 Antarctic sub-shelf melt rates via PICO. *Cryosphere* **12**, 1969–1985. (doi:10.5194/tc-12-1969-2018)
62. Lazeroms WMJ, Jenkins A, Gudmundsson GH, van de Wal RSW. 2018 Modelling present-day basal melt rates for Antarctic ice shelves using a parametrization of buoyant meltwater plumes. *Cryosphere* **12**, 49–70. (doi:10.5194/tc-12-49-2018)
63. Adusumilli S, Fricker HA, Medley B, Padman L, Siegfried MR. 2020 Interannual variations in meltwater input to the Southern Ocean from Antarctic ice shelves. *Nat. Geosci.* **13**, 616–620. (doi:10.1038/s41561-020-0616-z)
64. Rignot E, Jacobs S, Mouginot J, Scheuchl B. 2013 Ice-shelf melting around Antarctica. *Science* **341**, 266–270. (doi:10.1126/science.1235798)
65. Werder MA, Hewitt IJ, Schoof CG, Flowers GE. 2013 Modeling channelized and distributed subglacial drainage in two dimensions. *J. Geophys. Res.* **118**, 1–19. (doi:10.1002/jgrf.20146)
66. Dow CF, Werder MA, Babonis G, Nowicki S, Walker RT, Csatho B, Morlighem M. 2018 Dynamics of active subglacial lakes in Recovery Ice Stream. *J. Geophys. Res. Earth Surf.* **123**, 837–850. (doi:10.1002/2017JF004409)
67. Wilner JA, Morlighem M, Cheng G. 2023 Evaluation of four calving laws for Antarctic ice shelves. *Cryosphere Discuss.* **17**, 1–19. (doi:10.5194/tc-17-4889-2023)
68. Yu H, Rignot E, Seroussi H, Morlighem M, Choi Y. 2019 Impact of iceberg calving on the retreat of Thwaites Glacier, West Antarctica over the next century with different calving laws and ocean thermal forcing. *Geophys. Res. Lett.* **46**, 14539–14547. (doi:10.1029/2019gl084066)
69. Groh A, Horwath M. 2021 Antarctic ice mass change products from GRACE/GRACE-FO using tailored sensitivity kernels. *Remote Sens.* **13**, 1736. (doi:10.3390/rs13091736)
70. Zwally HJ, Giovinetto MB, Beckley MA, Saba JL. 2012 Antarctic and Greenland drainage systems. *GSFC Cryospher. Sci. Lab.* **265**.
71. Dow CF. 2022 The role of subglacial hydrology in Antarctic ice sheet dynamics and stability: a modelling perspective. *Ann. Glaciol.* **63**, 49–54. (doi:10.1017/aog.2023.9)
72. Greve R, Chambers C, Obase T, Saito F, Chan WL, Abe-Ouchi A. 2023 Future projections for the Antarctic ice sheet until the year 2300 with a climate-index method. *J. Glaciol.* **69**, 1569–1579. (doi:10.1017/jog.2023.41)
73. Horton BP, Khan NS, Cahill N, Lee JSH, Shaw TA, Garner AJ, Kemp AC, Engelhart SE, Rahmstorf S. 2020 Estimating global mean sea-level rise and its uncertainties by 2100 and 2300 from an expert survey. *Npj Clim. Atmos. Sci.* **3**, 18. (doi:10.1038/s41612-020-0121-5)
74. van de Wal RSW *et al*. 2022 A high-end estimate of sea level rise for practitioners. *Earths. Future* **10**, e2022EF002751. (doi:10.1029/2022EF002751)
75. Golledge NR, Kowalewski DE, Naish TR, Levy RH, Fogwill CJ, Gasson EGW. 2015 The multi-millennial Antarctic commitment to future sea-level rise. *Nature* **526**, 421–425. (doi:10.1038/nature15706)

76. Kopp RE, Horton RM, Little CM, Mitrovica JX, Oppenheimer M, Rasmussen DJ, Strauss BH, Tebaldi C. 2014 Probabilistic 21st and 22nd century sea-level projections at a global network of tide-gauge sites. *Earth's Future* **2**, 383–406. (doi:10.1002/2014ef000239)
77. Palmer MD *et al*. 2020 Exploring the drivers of global and local sea-level change over the 21st century and beyond. *Earths. Future* **8**, e2019EF001413. (doi:10.1029/2019EF001413)
78. The Intergovernmental Panel on Climate Change. 2023 Climate change 2021 – the physical science basis: working group I contribution to the sixth assessment report of the intergovernmental panel on climate change. In *Contribution of Working Group I to the Sixth Assessment Report of The Intergovernmental Panel on Climate Change*. (doi:10.1017/9781009157896)
79. Turner FE, Malagon Santos V, Edwards TL, Slangen ABA, Nicholls RJ, Le Cozannet G, O'Neill J, Adhikari M. 2023 Illustrative multi-centennial projections of global mean sea-level rise and their application. *Earths. Future* **11**, e2023EF003550. (doi:10.1029/2023EF003550)
80. Zhao C *et al*. 2025 Subglacial water amplifies Antarctic contributions to sea-level rise. *Nat. Commun*. **16**, 3187. (doi:10.1038/s41467-025-58375-4)
81. Pelle T, Greenbaum JS, Ehrenfeucht S, Dow CF, McCormack FS. 2024 Subglacial discharge accelerates dynamic retreat of aurora subglacial basin Outlet Glaciers, East Antarctica, Over the 21st Century. *J. Geophys. Res. Earth Surf.* **129**, e2023JF007513. (doi:10.1029/2023JF007513)
82. Gagliardini O, Cohen D, Råback P, Zwinger T. 2007 Finite-element modeling of subglacial cavities and related friction law. *J. Geophys. Res. Earth Surf.* **112**, 1–11. (doi:10.1029/2006JF000576)
83. Jenkins A. 2011 Convection-driven melting near the grounding lines of ice shelves and tidewater glaciers. *J. Phys. Oceanogr*. **41**, 2279–2294. (doi:10.1175/jpo-d-11-03.1)
84. Le Brocq AM *et al*. 2013 Evidence from ice shelves for channelized meltwater flow beneath the Antarctic Ice Sheet. *Nat. Geosci*. **6**, 945–948. (doi:10.1038/ngeo1977)
85. Marsh OJ, Fricker HA, Siegfried MR, Christianson K, Nicholls KW, Corr HFJ, Catania G. 2016 High basal melting forming a channel at the grounding line of Ross Ice Shelf, Antarctica. *Geophys. Res. Lett*. **43**, 250–255. (doi:10.1002/2015gl066612)
86. Alley KE, Scambos TA, Siegfried MR, Fricker HA. 2016 Impacts of warm water on Antarctic ice shelf stability through basal channel formation. *Nat. Geosci*. **9**, 290–293. (doi:10.1038/ngeo2675)
87. Wei W *et al*. 2020 Getz Ice Shelf melt enhanced by freshwater discharge from beneath the West Antarctic Ice Sheet. *Cryosphere* **14**, 1399–1408. (doi:10.5194/tc-14-1399-2020)
88. Gwyther DE, Dow CF, Jendersie S, Gourmelen N, Galton-Fenzi BK. 2023 Subglacial freshwater drainage increases simulated basal melt of the Totten Ice Shelf. *Geophys. Res. Lett*. **50**, e2023GL103765. (doi:10.1029/2023GL103765)
89. Nakayama Y, Cai C, Seroussi H. 2021 Impact of subglacial freshwater discharge on Pine Island Ice Shelf. *Geophys. Res. Lett*. **48**, e2021GL093923. (doi:10.1029/2021GL093923)
90. Ehrenfeucht S, Dow C. 2025 Impacts of bed topography resolution on sea-level rise projections from coupled subglacial hydrology and ice dynamics for Thwaites Glacier, Antarctica. Dryad Digital Repository. (doi:10.5061/dryad.xd2547dvb)
91. Ehrenfeucht S, Dow C. 2026 Supplementary material from: Impacts of bed topography resolution on sea-level rise projections from coupled subglacial hydrology and ice dynamics for Thwaites Glacier, Antarctica. Figshare. (doi:10.6084/m9.figshare.c.8375226)